ACS APPLIED MATERIALS & INTERFACES

CALTECH LIBRARY SERVICES

Subscriber access provided by Caltech Library Services

Article

Structure and Failure Mechanism of the Thermoelectric CoSb/TiCoSb Interface

Guodong Li, Shiqiang Hao, Umut Aydemir, Max Wood, William A. Goddard, Pengcheng Zhai, Qingjie Zhang, and Gerald Jeffrey Snyder

ACS Appl. Mater. Interfaces, **Just Accepted Manuscript** • DOI: 10.1021/acsami.6b07320 • Publication Date (Web): 01 Nov 2016

Downloaded from http://pubs.acs.org on November 3, 2016

Just Accepted

"Just Accepted" manuscripts have been peer-reviewed and accepted for publication. They are posted online prior to technical editing, formatting for publication and author proofing. The American Chemical Society provides "Just Accepted" as a free service to the research community to expedite the dissemination of scientific material as soon as possible after acceptance. "Just Accepted" manuscripts appear in full in PDF format accompanied by an HTML abstract. "Just Accepted" manuscripts have been fully peer reviewed, but should not be considered the official version of record. They are accessible to all readers and citable by the Digital Object Identifier (DOI®). "Just Accepted" is an optional service offered to authors. Therefore, the "Just Accepted" Web site may not include all articles that will be published in the journal. After a manuscript is technically edited and formatted, it will be removed from the "Just Accepted" Web site and published as an ASAP article. Note that technical editing may introduce minor changes to the manuscript text and/or graphics which could affect content, and all legal disclaimers and ethical guidelines that apply to the journal pertain. ACS cannot be held responsible for errors or consequences arising from the use of information contained in these "Just Accepted" manuscripts.

ACS Publications

ACS Applied Materials & Interfaces is published by the American Chemical Society. 1155 Sixteenth Street N.W., Washington, DC 20036

Published by American Chemical Society. Copyright © American Chemical Society. However, no copyright claim is made to original U.S. Government works, or works produced by employees of any Commonwealth realm Crown government in the course of their duties.

Structure and Failure Mechanism of the Thermoelectric $CoSb_3$/TiCoSb Interface

Guodong Li [†,‡], Shiqiang Hao [‡], Umut Aydemir [‡], Max Wood [‡], William A. Goddard III [⊥], Pengcheng Zhai [†], Qingjie Zhang [*,†], and G. Jeffrey Snyder [*,‡,§]

[†]State Key Laboratory of Advanced Technology for Materials Synthesis and Processing, Wuhan University of Technology, Wuhan 430070, China.

[‡]Department of Materials Science and Engineering, Northwestern University, Evanston, Illinois 60208, USA.

[⊥]Materials and Process Simulation Center, California Institute of Technology, Pasadena, California 91125, USA.

[§]ITMO University, St. Petersburg, Russia

[*]Corresponding authors: jeff.snyder@northwestern.edu; zhangqj@whut.edu.cn

Abstract: The brittle behavior and low strength of $CoSb_3$/TiCoSb interface are serious issues concerning the engineering applications of $CoSb_3$ based or $CoSb_3$/TiCoSb segmented thermoelectric devices. To illustrate the failure mechanism of the $CoSb_3$/TiCoSb interface, we apply density functional theory to investigate the interfacial behavior and examine the response during tensile deformations. We find that both $CoSb_3$(100)/TiCoSb(111) and $CoSb_3$(100)/TiCoSb(110) are energetically favorable interfacial structures. Failure of the $CoSb_3$/TiCoSb interface occurs in $CoSb_3$ since the structural stiffness of $CoSb_3$ is much weaker than that of TiCoSb. This failure within $CoSb_3$ can be explained through the softening of the Sb−Sb bond along with the cleavage of the Co−Sb bond in the interface. The failure mechanism the $CoSb_3$/TiCoSb interface is similar to that of bulk $CoSb_3$, but the ideal tensile strength and failure strain of the $CoSb_3$/TiCoSb interface are much lower than those of bulk $CoSb_3$. This can be attributed to the weakened stiffness of the Co−Sb framework due to structural rearrangement near the interfacial region.

Keywords: thermoelectric; interfacial structure; tensile failure mode; ideal strength; bond breakage

1. INTRODUCTION

Solid-state thermoelectric (TE) power generation devices can directly convert heat into electricity with high reliability and no moving parts. Thermoelectrics have been used to power space-crafts for deep-space missions for decades and are being currently considered for

applications in recovery of automobile exhaust heat.[1] To achieve high efficiency in thermal-to-electrical energy conversion, TE materials with high figure-of-merit (zT) are needed. $CoSb_3$ based TE devices have high potential for engineering applications because both n- and p-type doped $CoSb_3$ demonstrate excellent figure of merit ($zT > 1$) in the intermediate temperature region (500 – 750 K). [2-7] Meanwhile, Half-Heusler compounds such as *X*NiSn and *X*CoSb (*X* = Ti, Zr, Hf) have peak TE properties in a higher temperature range (750 – 900 K).[8-10] Designing segmented TE devices with various TE materials (*e.g.*, $CoSb_3$/TiCoSb TE devices) in their respective temperature ranges results in an overall high TE efficiency,[11] but also creates new interfaces such as $CoSb_3$/TiCoSb interface.

In designing TE devices, it is important to find a proper contacting material to form leg-electrode interfaces. For $CoSb_3$ based TE devices, Ti has been confirmed to be a good joint forming metal.[12-16] Bae *et al*. investigated the adhesion properties of $CoSb_3$/Ti/Mo(Cu) interfaces and found that a Ti interlayer is a potential candidate for making a reliable $CoSb_3$ based unicouple with high adhesion strength.[12] Later Zhao *et al*. investigated the interfacial behavior of $CoSb_3$/Ti after thermal aging and observed the formation of a multi-layer interfacial structure composed of $CoSb_3$/TiCoSb/$TiSb_2$/TiSb/Ti.[13-16] At the $CoSb_3$/Ti interface, TiSb layer initially formed during spark plasma sintering (SPS). With the aging time increased, Sb decomposed from $CoSb_3$ layer would react with TiSb phase, leading to the formation of $TiSb_2$ layer ($Sb + TiSb \rightarrow TiSb_2$). Consequently, Ti atoms diffused into $CoSb_3$/$TiSb_2$ interface to form TiCoSb layer ($Ti + CoSb_3 \rightarrow$ TiCoSb). The formation of $CoSb_3$/TiCoSb/$TiSb_2$/TiSb/Ti, which is mainly due to the mutual diffusion of Sb and Ti elements,[15] suggests the presence of a good electrical contact between the $CoSb_3$/TiCoSb interface.[13-16]

However, the mechanical reliability of $CoSb_3$ based or $CoSb_3$/TiCoSb segmented TE devices is a serious consideration for their applications.[17] For example, the difference in the coefficient of thermal expansion (CTE) between $CoSb_3$ and TiCoSb can easily generate significant thermo-mechanical stresses, leading to cracks close to the $CoSb_3$/TiCoSb interface, resulting in the failure of TE devices.[13-16] Moreover, the CTE of TiCoSb changes at different temperatures,[18] which could also lead to significant thermo-mechanical stresses if a TE device is subjected to severe operational conditions. Due to the cyclic thermal loading of $CoSb_3$/TiCoSb segmented thermoelectric (TE) device, the $CoSb_3$/TiCoSb interface is subjected to cyclic tension – compression stresses, which inevitably weakens the $CoSb_3$/TiCoSb interface. Therefore, understanding the interfacial tensile failure mechanism between $CoSb_3$ and TiCoSb is an essential first step for developing $CoSb_3$ based or $CoSb_3$/TiCoSb segmented TE devices.

In order to understand the interfacial behavior and illustrate the intrinsic failure mechanism of the $CoSb_3$/TiCoSb interface, we investigated the interfacial structure and examined the response along tensile deformations using density functional theory. We first studied the surface energies of many possible surface configurations of $CoSb_3$ and TiCoSb, and found that the $CoSb_3$(100), TiCoSb(110) and TiCoSb(111) surfaces are the most energetically favorable, with surface energies of 0.812, 1.758, and 1.785 J/m^2, respectively. We further found that both $CoSb_3$(100)/TiCoSb(111) and $CoSb_3$(100)/TiCoSb(110) interfaces are the most favorable interfacial structures. Based on our analysis, the initial crack formation of the $CoSb_3$/TiCoSb interface occurs in $CoSb_3$, and arises from the softening of the Sb–Sb bond followed by the cleavage of the Co–Sb bond. As described in our previous study on $CoSb_3$,[19] the calculated force constant for the Sb–Sb bond is much lower than that of the Co–Sb bond, suggesting that the covalent Sb–Sb interactions are much weaker than the ionic interactions between the Co and Sb atoms. However, the ideal tensile strength and failure strain of the $CoSb_3$/TiCoSb interface are much lower than those of bulk $CoSb_3$. We consider that these findings on the $CoSb_3$/TiCoSb interface system may shed some light on the design issues encountered during the development of other segmented TE devices.

This study explains on an atomic level the intrinsic tensile failure mechanism of the $CoSb_3$/TiCoSb interface, providing a fundamental understanding of the structure-chemical bonding relationship. We believe this is an essential first step for comprehensively understanding the failure of the $CoSb_3$/TiCoSb interface, which will lay the essential foundation for developing segmented TE materials with excellent mechanical properties.

2. METHODOLOGY

The Vienna *ab initio* Simulation Package (VASP) was used for all density functional theory (DFT) calculations, which were carried out using the Perdew-Burke-Ernzerhof (PBE) exchange-correlation functional with the projector augmented wave (PAW) method to deal with the core-valence interactions.[20-22] The convergence criteria were set to 1×10^{-6} eV energy difference for solving the electronic wave function and 1×10^{-2} eV/Å force for geometry optimization. The convergence test showed that a plane wave cutoff energy of 500 eV gives a good convergence for the total energies. To minimize the total energy of the $CoSb_3$ and TiCoSb bulk systems, a 7×7×7 Monkhorst-Pack uniform *k*-point reciprocal space sampling was adopted to fully optimize the internal coordinates of the atoms. Our optimized lattice parameter for $CoSb_3$ is a = 9.048 Å, which is only 0.01% larger than the experimental value of 9.039 Å.[23] Our optimized lattice

parameter for TiCoSb is a = 5.855 Å, which is only 0.48% smaller than the experimental value of 5.883 Å.[24] These calculated values are in good agreement with the previously published theoretical value of 9.14 Å for $CoSb_3$ and 5.89 Å for TiCoSb.[25-27]

To determine the favorable surface slab, we calculated the surface energy, γ, from the following expression,[28,29]

$$\gamma = \frac{E_{slab} - N \cdot E_{bulk}}{2A} \quad (1)$$

where: E_{slab} is the total energy of surface slab obtained from density functional theory calculations, N is the number of atoms in the surface slab, E_{bulk} is the bulk energy per atom, and A is the surface area.

In order to determine the low energy interfacial structures, we calculated the interfacial formation energy E_f from the following expression,[28,29]

$$E_f = \frac{E_{inter} - \sum_i E^i_{slab}}{S} \quad (2)$$

where: E_{inter} is the total energy of the $CoSb_3$/TiCoSb interfacial system, E^i_{slab} is the energy of the i slab (i = $CoSb_3$, TiCoSb), and is the interface area. For all interfacial structures described below, the gamma only k-point sampling was used to minimize the total energy.

To examine the tensile deformation mechanism of the $CoSb_3$/TiCoSb interface, we imposed the uniaxial tensile strain on a particular direction while allowing structural relaxation along the other five strain components. The residual stresses for relaxation of these five strain directions are all less than 0.5 GPa. We applied a small uniaxial tensile strain to the supercell configuration relaxed in the previous step in order to obtain stress-strain curves. A 1% level of strain was predefined as the small strain increment for each deformation step. The stress is defined as the force per deformed area, and the strain is defined as the true strain. This relaxation method has been proven to be an effective tool to calculate the ideal strength, and sheds light on the intrinsic failure mechanism at the atomistic scale.[30-32] The tensile stress σ_{ij} was calculated by,[33]

$$\sigma_{ij} = \frac{1}{V}\left(\frac{\partial U}{\partial \varepsilon_{ij}}\right) \quad (3)$$

where: U is the total (or internal) energy of the system, V is the system volume under strain, and ε_{ij} is the infinitesimal strain.

3. RESULTS AND DISCUSSION

3.1 Crystal structures of $CoSb_3$ and TiCoSb

Skutterudite $CoSb_3$ crystallizes in a cubic lattice (space group *Im*-3 (204), a = 9.0385 Å), in which the unit cell contains 8 Co and 24 Sb atoms occupying the 8*c*- and the 24*g*-sites, respectively (Figure 1(a)).[23] The Co atoms form a simple cubic framework within which 4 Sb atoms are arranged into a planar rectangular ring. There are 6 such rings in the unit cell, but two of the eight Co cubes remain empty, giving rise to two void cages.

The Half-Heusler TiCoSb compound forms a cubic structure with space group $F\bar{4}3m$, where Ti and Sb atoms form a NaCl-type framework, while the Co atoms replace the Zn atoms in ZnS-type sub-structure.[34] As shown in Figure 1(b), the Ti and Sb atoms form TiSb cubic frameworks within which one Co atom is located in the center. There are four such frameworks, but the other four TiSb cubes have one vacancy site in the center, giving rise to unoccupied space in the unit cell.

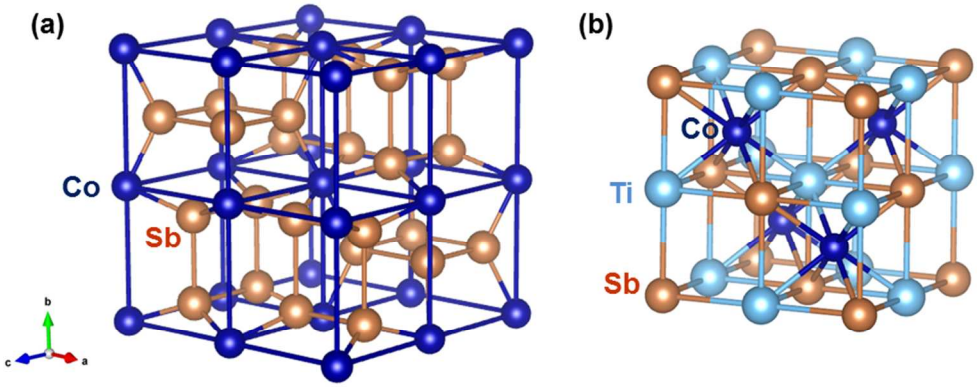

Figure 1. Atomic structures of (a) $CoSb_3$ and (b) TiCoSb. The Co, Sb, and Ti atoms are represented with dark-blue, brown, and light-blue spheres, respectively.

3.2 Favorable slabs in $CoSb_3$ and TiCoSb

We considered three slab systems for fcc $CoSb_3$ and TiCoSb to calculate the surface energy:

- Both $CoSb_3$(100) and TiCoSb (100) with lattice orientation (*a*, *b*, *c*) along (<010>, <001>, <100>). Specifically, $CoSb_3$(100) oriented unit cell contains 32 atoms with the lattice parameter $a = b = c$ = 9.048 Å. TiCoSb (100) oriented unit cell contains 12 atoms with the lattice parameter $a = b = c$ = 5.855 Å.
- Both $CoSb_3$(110) and TiCoSb (110) with lattice orientation (*a*, *b*, *c*) along (<1-10>, <00-1>, <110>). Specifically, $CoSb_3$(110) oriented unit cell contains 32 atoms with the lattice

parameter a = 12.80 Å, b = 9.048 Å, c = 6.398 Å. TiCoSb (110) oriented unit cell contains 12 atoms with the lattice parameter a = 8.280 Å, b = 5.855 Å, c = 4.140 Å.

- Both $CoSb_3$(111) and TiCoSb (111) with lattice orientation (a, b, c) along (<1-10>, <11-2>, <111>). Specifically, $CoSb_3$(111) oriented unit cell contains 64 atoms with the lattice parameter a = 12.80 Å, b = 22.16 Å, c = 5.224 Å. TiCoSb (111) oriented unit cell contains 24 atoms with the lattice parameter a = 8.280 Å, b = 14.34 Å, c = 3.38 Å.

In all the slab systems, c oriented slabs are considered. That is, all the slab systems are along the c direction, which is surrounded by a vacuum region of 20 Å to decouple the slab. The energy of a surface depends on the dangling bonds on the surface.[35] Thus, the lowest energy and therefore most likely surface structure of each slab is the one that leaves minimum number of dangling bonds. Then, all the surface atoms are fully relaxed to optimize the surface structure. Here, the surface reconstruction is not considered because there is no experimental guidance. For $CoSb_3$, the (3×3×1), (3×3×1), and (3×1×1) Monkhorst-Pack k-point reciprocal space sampling was adopted for the (100), (110), and (111) oriented surfaces, respectively. Here, we did a k-point convergence test for the (111) oriented $CoSb_3$ surface, and found that the free energy (-613.042 eV) using (3×1×1) k-point sampling is nearly the same as that using (4×2×2) k-point sampling (-613.040 eV). We believe that a (3×1×1) k-point sampling gives a good convergence. For TiCoSb, the (5×5×2), (4×5×2), and (4×2×2) k-point sampling was adopted for the (100), (110), and (111) oriented surfaces, respectively. The slabs with 2 unit layers were used to calculate the surface energy. The surface energies of typical low-index surfaces in $CoSb_3$ and TiCoSb are listed in Table 1. For $CoSb_3$, it clearly shows that the (100) oriented surface has the lowest surface energy of 0.812 J/m^2, indicating $CoSb_3$(100) is the favorable slab, as shown in Figure 2. For TiCoSb, the surface energy of the (110) and (111) oriented surfaces are much lower than that of the (100) oriented surface, suggesting that both TiCoSb(110) and TiCoSb(111) are the most favorable slabs, as shown in Figure 3 and 4.

Table 1. Calculated surface energies, γ, for various $CoSb_3$ and TiCoSb surfaces.

	$CoSb_3$			**TiCoSb**		
Surface	(100)	(110)	(111)	(100)	(110)	(111)
Surface energy (J/m^2)	0.812	1.178	0.978	2.046	1.758	1.785

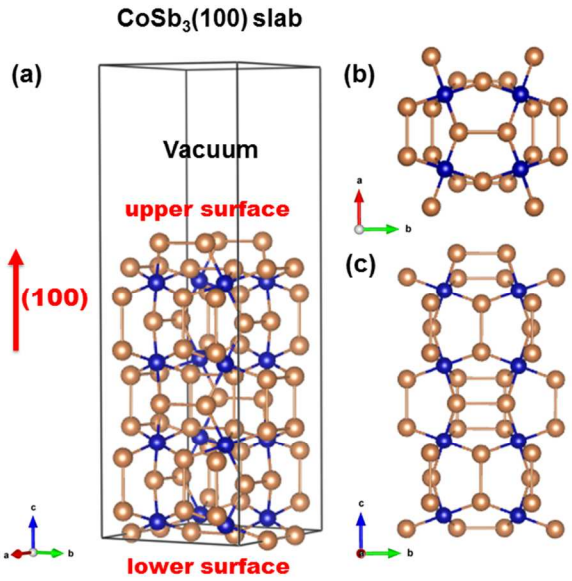

Figure 2. (a) The $CoSb_3$(100) slab structure with 2 unit layers in a = 18.096 Å, (b) Bottom view of the $CoSb_3$(100) slab, and (c) Front view of the $CoSb_3$(100) slab. The Co and Sb atoms are represented with dark-blue and brown spheres, respectively.

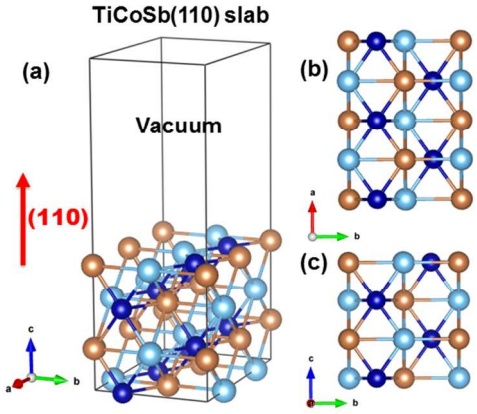

Figure 3. (a) The TiCoSb(110) slab structure with 2 unit layers in a = 8.18 Å, (b) Bottom view of the TiCoSb(110) slab, (c) Front view of the TiCoSb(110) slab. The Co, Sb, and Ti atoms are represented with dark-blue, brown, and light-blue spheres, respectively.

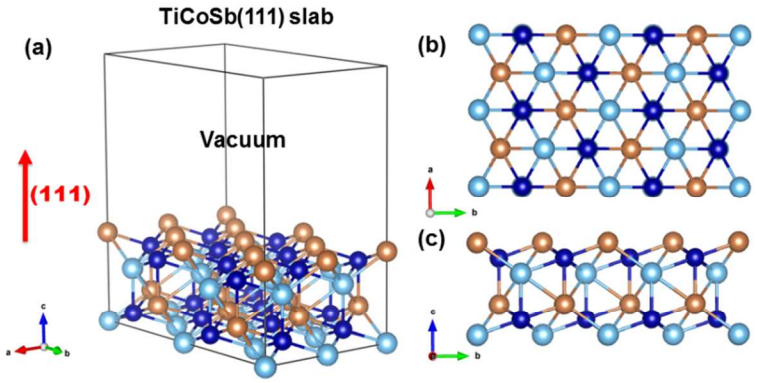

Figure 4. (a) The TiCoSb(111) slab structure with 2 unit layers in a = 6.76 Å, (b) Bottom view of the TiCoSb(111) slab, and (c) Front view of the TiCoSb(111) slab. The Co, Sb, and Ti atoms are represented with dark-blue, brown, and light-blue spheres, respectively.

3.3 Low energy interfacial structures of $CoSb_3$/TiCoSb

As $CoSb_3$(100), TiCoSb(111) and TiCoSb(110) are favorable slabs, $CoSb_3$(100)/TiCoSb(111) and $CoSb_3$(100)/TiCoSb(110) interfacial structures are considered in this study. For the $CoSb_3$(100) slab shown in Figure 2, due to different Sb atomic structures on the upper and lower slab, we consider two types of structures for each $CoSb_3$/TiCoSb interface: upper_$CoSb_3$/TiCoSb and lower_$CoSb_3$/TiCoSb. In total, we can build four interfacial structures, namely upper_$CoSb_3$(100)/TiCoSb(111), lower_$CoSb_3$(100)/TiCoSb(111), upper_$CoSb_3$(100)/TiCoSb(110), and lower_$CoSb_3$(100)/TiCoSb(110). The detailed explanation of these four interfacial structures is illustrated in the supporting information (Figures S1-S4). The $CoSb_3$(100)/TiCoSb(111) interface consists of a (1×3)-$CoSb_3$(100) cell (a = 9.048 Å, b = 27.144 Å) and a (1×2)-TiCoSb(111) cell (a = 8.280 Å, b = 28.680 Å) with 276 atoms in the system. We keep the lateral lattice parameter of the interface fixed for the $CoSb_3$(100) cell, which leads to a mismatch with the TiCoSb(111) cell of 8.5% along the a direction and 5.7% along the b direction. Here, we remove equivalent Ti, Co, and Sb atoms in the TiCoSb(111) cell to eliminate unfavorable neighboring atomic interactions with bonding distances less than 1.5 Å around the interface boundary. The $CoSb_3$(100)/TiCoSb(110) interface consists of a (1×2)-$CoSb_3$(100) cell (a = 9.048 Å, b = 18.096 Å) and a (1×3)- TiCoSb(110) cell (a = 8.28 Å, b = 17.565 Å) with 200 atoms in the system. Again we keep the lateral lattice parameter of the interface fixed for the $CoSb_3$(100) cell, resulting in a mismatch with the TiCoSb(110) cell of 8.5% along the a direction and 2.9% along the b direction. Among all structures, a vacuum region of 10

Å surrounds the unit cell edge along the c direction. It should be noted that no experimental study is available in literature that may guide us to understand how the $CoSb_3$ and TiCoSb slabs cohere together. Therefore, we theoretically consider several possible coherent structures for each interface and choose the lowest energy structure as the favorable one. Obviously, the favorable interface is much easier to form compared with the other interfaces with higher formation energies. The details of modeling these interfaces are illustrated in the supporting information (Figures S5-S8). Table 2 lists the calculated interfacial formation energies for various possible interfacial structures of $CoSb_3$/TiCoSb shown in Figures S5-S8, and Figures 5-8 show the favorable structures of each kind of $CoSb_3$/TiCoSb interface. There are many more bonds in the $CoSb_3$(100)/TiCoSb(111) interfacial regions compared with the $CoSb_3$(100)/TiCoSb(110) interfacial regions (Figures 5-8), indicating the $CoSb_3$(100)/TiCoSb(111) interfaces are more favorable. This can be also be verified by noting the lower formation energies of the $CoSb_3$(100)/TiCoSb(111) interfaces compared with those of the $CoSb_3$(100)/TiCoSb(110) interfaces (see Table 2). However, the formation energies of the $CoSb_3$(100)/TiCoSb(110) interfaces are only 0.03 and 0.04 J/m^2 for upper one and lower one, respectively, suggesting that they can be favorable as well. Thus, all the structures shown in Figures 5-8 will be considered to illustrate the failure mechanism of the $CoSb_3$/TiCoSb interface.

Table 2. Interfacial formation energies (E_f in J/m^2) calculated for all possible $CoSb_3$/TiCoSb interfacial structures. The lowest formation energies are indicated in bold type, and the corresponding interface structure is shown in Figures 5-8.

Configurations	**Possible structures and formation energies (E_f)**									
	1	2	3	4	5	6	7	8	9	10
upper_$CoSb_3$(100)/TiCoSb(111)	-0.20	-0.22	-0.24	-0.29	-0.21	-0.35	**-0.36**	-0.29		
lower_$CoSb_3$(100)/TiCoSb(111)	-0.41	-0.41	-0.41	**-0.54**	-0.46	-0.46	-0.46	-0.42	-0.46	-0.45
upper_$CoSb_3$(100)/TiCoSb(110)	0.14	0.13	0.11	0.07	0.06	**0.03**	0.04			
lower_$CoSb_3$(100)/TiCoSb(110)	0.15	0.07	0.07	0.11	**0.04**	0.09	0.07	0.05	0.09	0.11

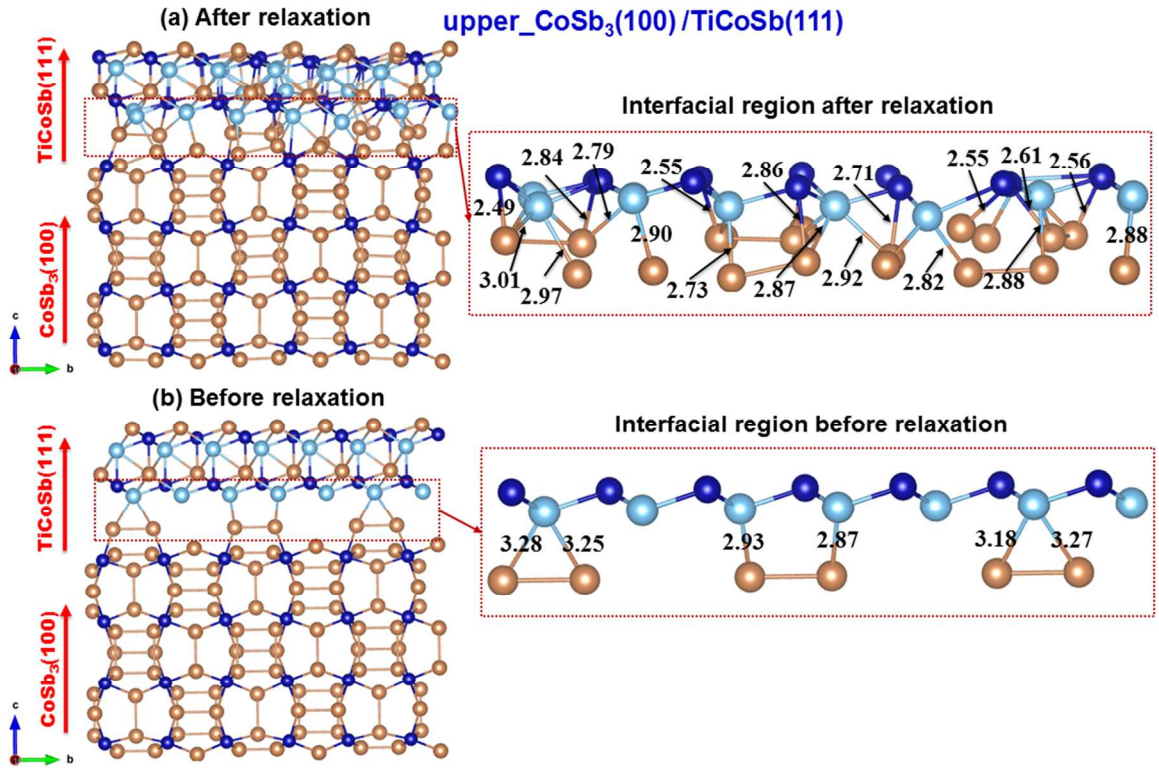

Figure 5. The interfacial structure which has the lowest interfacial formation energy in all possible upper_$CoSb_3$(100)/TiCoSb(111) structures, (a) After relaxation, (b) before relaxation. The main bond lengths before/after atomic rearrangement are shown in the zoomed interfacial region. The unit of the bond length is Å. The Co, Sb, and Ti atoms are represented with dark-blue, brown, and light-blue spheres, respectively.

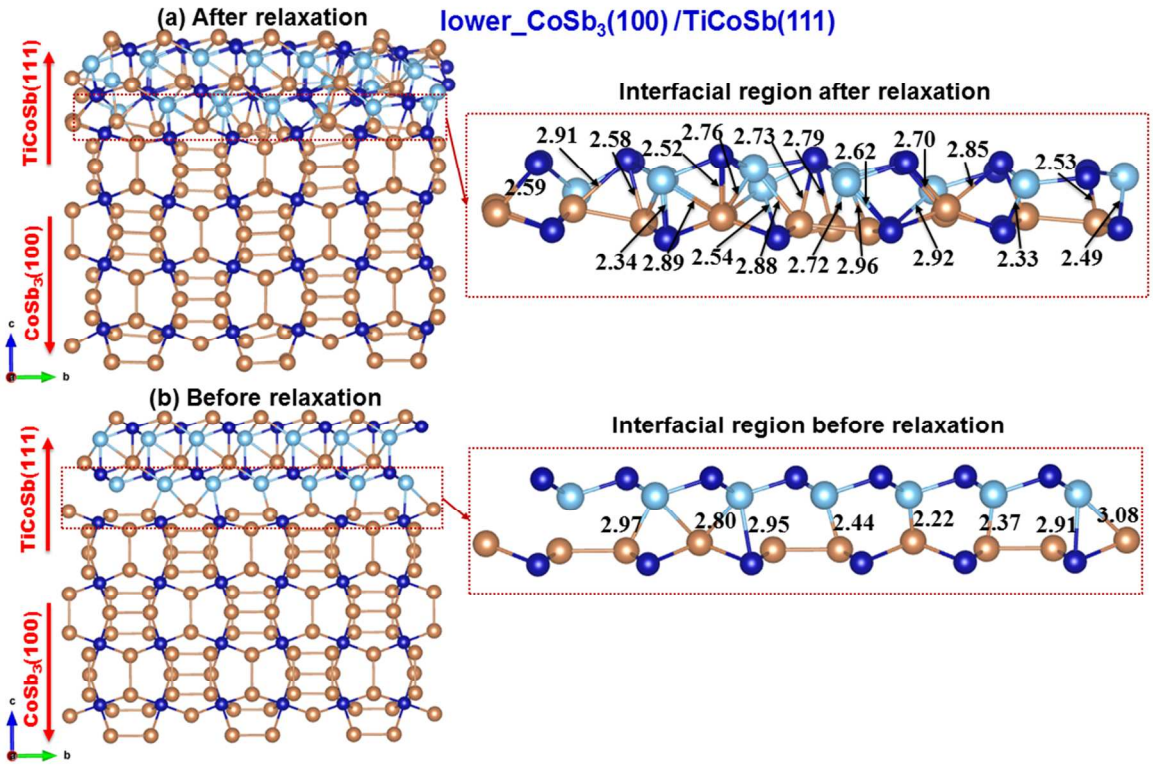

Figure 6. The interfacial structure which has the lowest interfacial formation energy in all possible lower_$CoSb_3$(100)/TiCoSb(111) structures, (a) After relaxation, (b) before relaxation. The main bond lengths before/after atomic rearrangement are shown in the zoomed interfacial region. The unit of the bond length is Å. The Co, Sb, and Ti atoms are represented with dark-blue, brown, and light-blue spheres, respectively.

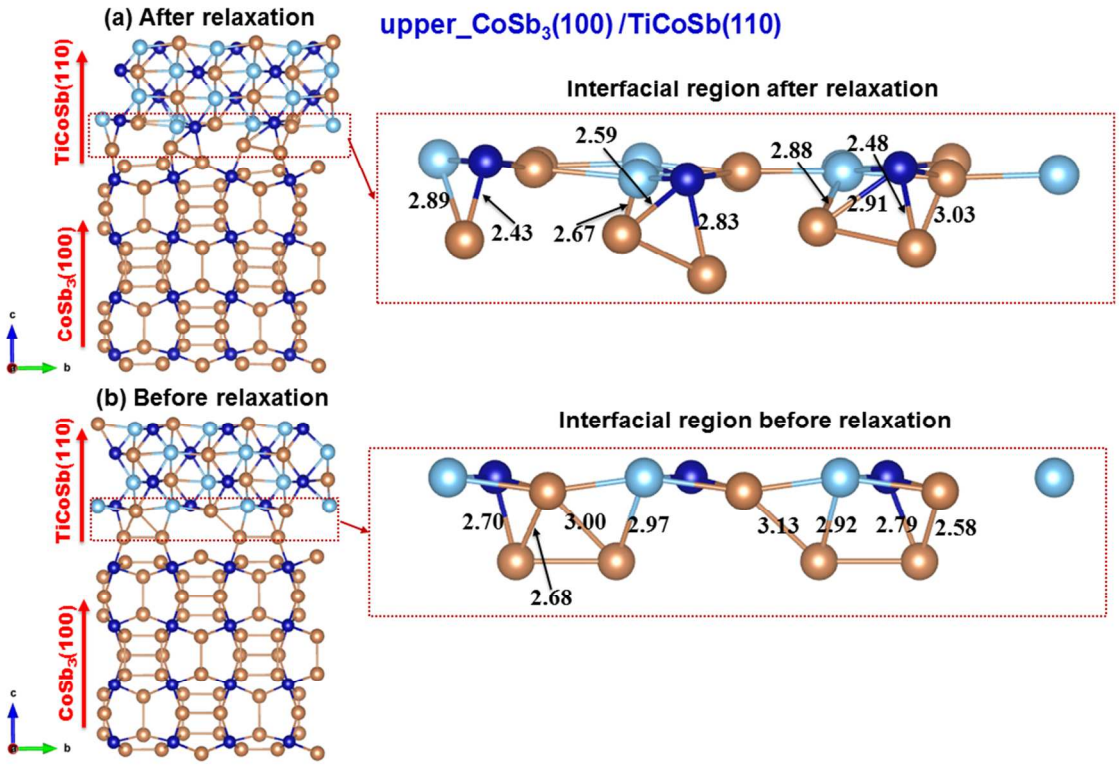

Figure 7. The interfacial structure which has the lowest interfacial formation energy in all possible upper_$CoSb_3$(100)/TiCoSb(110) structures, (a) After relaxation, (b) before relaxation. The main bond lengths before/after atomic rearrangement are shown in the zoomed interfacial region. The unit of the bond length is Å. The Co, Sb, and Ti atoms are represented with dark-blue, brown, and light-blue spheres, respectively.

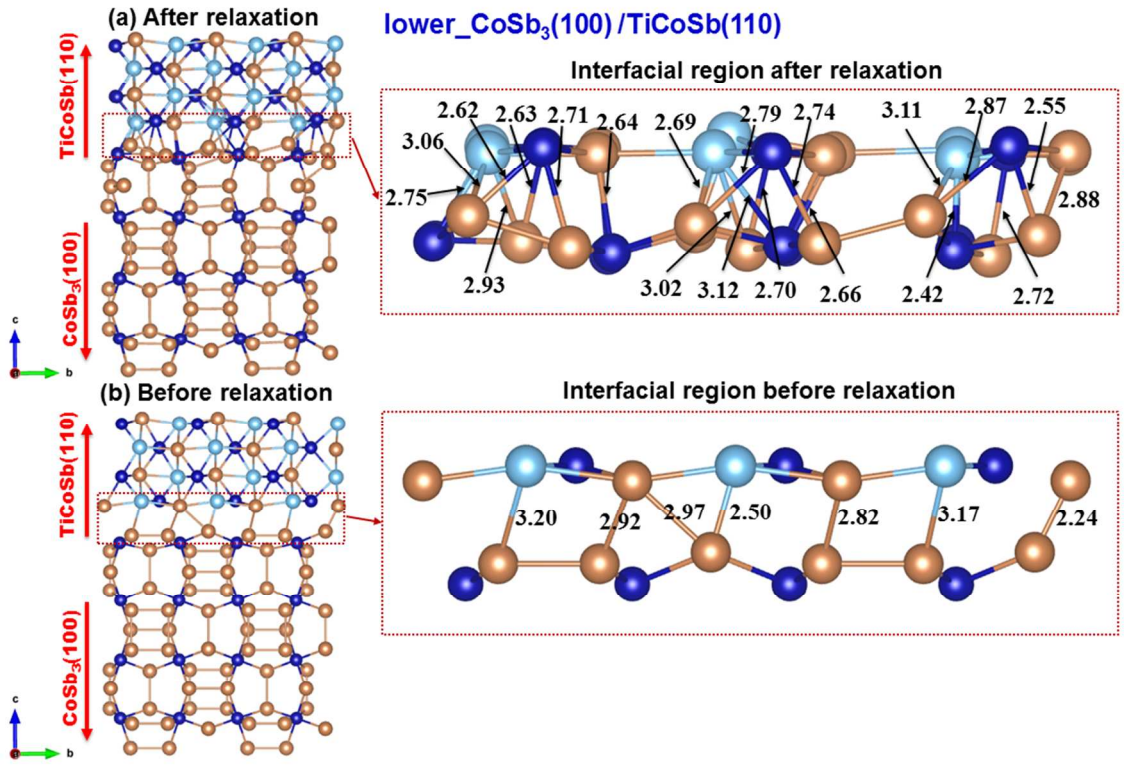

Figure 8. The interfacial structure which has the lowest interfacial formation energy in all possible lower_$CoSb_3$(100)/TiCoSb(110) structures, (a) After relaxation, (b) before relaxation. The main bond lengths before/after atomic rearrangement are shown in the zoomed interfacial region. The unit of the bond length is Å. The Co, Sb, and Ti atoms are represented with dark-blue, brown, and light-blue spheres, respectively.

3.4 Tension induced failure mechanism of the $CoSb_3$/TiCoSb interface

3.4.1 Ideal tensile strength of the $CoSb_3$/TiCoSb interface

The calculated tensile stress-strain relationships are investigated to understand the ideal tensile strength of the $CoSb_3$/TiCoSb interface, as shown in Figure 9. Here, we also calculated the corresponding bulk stress-strain responses as embedded in Figure 9. The ideal tensile strength of the $CoSb_3$(100)/TiCoSb(111) interface is calculated to be 7.92 GPa and 8.05 GPa for the upper and lower one, respectively, which is higher than that of the $CoSb_3$(100)/TiCoSb(110) interface (4.80 GPa for the upper one and 6.54 GPa for the lower one). The formation energy of the $CoSb_3$(100)/TiCoSb(111) interface is lower than that of the $CoSb_3$(100)/TiCoSb(110) interface (as listed in Table 2), which leads to a more favorable coherent structure in the $CoSb_3$(100)/TiCoSb(111) interface. This results in a much stronger resistance to the external tensile deformation and a much higher ideal strength of the $CoSb_3$(100)/TiCoSb(111) interface as

observed in Figure 5 and 6. Moreover, the fewer number of bonds in the upper_$CoSb_3$(100)/TiCoSb(110) interfacial region (Figure 7) leads to the weakest resistance against tension and the lowest ideal tensile strength of 4.80 GPa. The ideal tensile strength and fracture strain of various $CoSb_3$/TiCoSb interfaces are much lower than those of the bulk $CoSb_3$ and TiCoSb systems, indicating that the $CoSb_3$/TiCoSb interface fails more easily compared to the corresponding bulk systems.

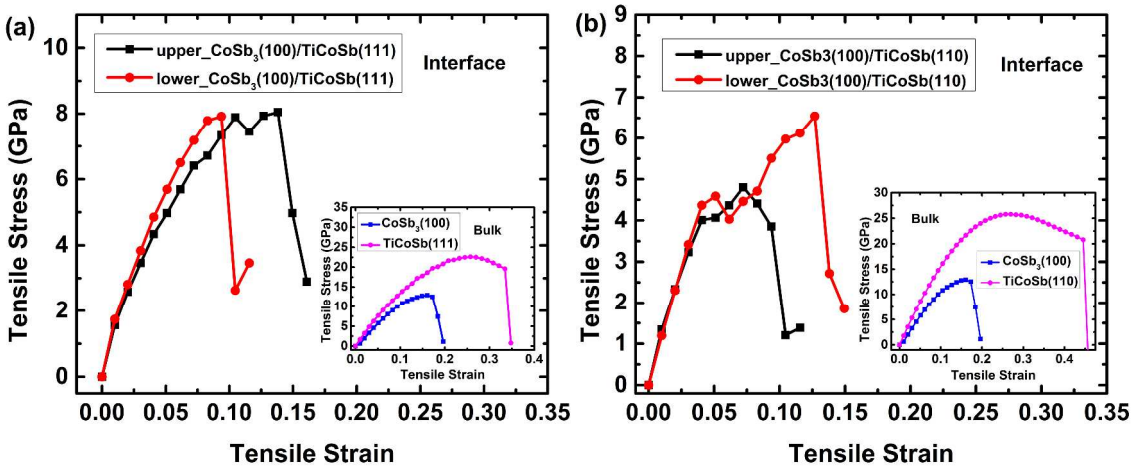

Figure 9. Calculated tensile stress as a function of tensile strain for various $CoSb_3$/TiCoSb interfaces: (a) $CoSb_3$(100)/TiCoSb(111) interfaces and the corresponding bulk systems, (b) $CoSb_3$(100)/TiCoSb(110) interfaces and the corresponding bulk systems.

3.4.2 Structure and bonding analysis of the $CoSb_3$/TiCoSb interface

The atomic configurations and the typical bond lengths under tensile deformations are extracted to understand the tension induced failure mechanism of the $CoSb_3$/TiCoSb interface, as shown in Figures 10-13. Figure 10 displays the structural deformations of the upper_$CoSb_3$(100)/TiCoSb(111) interface before and at the failure strain. The failure of the $CoSb_3$/TiCoSb interface occurs in $CoSb_3$, which agrees well with experimental observations.[16] The structure of TiCoSb is uniformly stretched to resist deformation until structural failure, suggesting a much stronger rigidity of TiCoSb compared to that of $CoSb_3$. This agrees with our prediction that the ideal tensile strength of TiCoSb is much higher than that of $CoSb_3$ as shown in Figure 9. At a tensile strain of 0.138, which corresponds to the ideal tensile strength, the Sb–Sb bond in $CoSb_3$ such as Sb1–Sb2, Sb3–Sb4 and Sb5–Sb6 softens, as highlighted in Figure 10(a),

but the Co−Sb framework still holds together. This can be attributed to the weaker rigidity of covalent Sb−Sb bond compared with that of the ionic Co−Sb bond in $CoSb_3$.[19] When tensile strain reaches 0.149, the Co−Sb framework no longer resists external deformation and begins to fail. The Co−Sb bond around the interfacial region breaks, releasing the tensile stress, and leads to failure of the interface. The failure mechanism of the $CoSb_3$/TiCoSb interface is similar to that of bulk $CoSb_3$.[19] The typical bond lengths of Sb1−Sb2, Sb3−Sb4, Sb5−Sb6, Co1−Sb7, Co2−Sb8, and Co3−Sb9 at various tensile strains are plotted in Figure 10(c). As the tensile strain increases to 0.105, Sb1−Sb2, Sb3−Sb4, and Sb5−Sb6 bonds are slightly stretched with the bond lengths changing from ~2.96 to ~3.06 Å. At a tensile strain of 0.116, these bond lengths increase to 3.10, 3.14, and 3.13 Å respectively, indicating a weaker or nonbonding Sb−Sb interaction as discussed previously.[36] This explains the decreasing tensile stress at this strain shown in Figure 9(a). However, the weaker or nonbonding Sb−Sb interaction only slightly releases the internal stress because the Co−Sb bond length decreases slightly, suggesting the Co−Sb framework can continue to resist the tensile deformation. With further increasing strain to 0.138, the Co3−Sb9 bond is stretched from 2.51 to 2.90 Å, with a stretching ratio of 15.54% before the failure, indicating a highly softened bond. Co1−Sb7 and Co2−Sb8 bond lengths increase from 2.42 and 2.46 Å to 2.62 and 2.58 Å with a stretching ratio of 8.26% and 4.88%, respectively. At the fracture strain of 0.149, the Co1−Sb7, Co2−Sb8, and Co3−Sb9 interatomic distances sharply increase to 4.51, 3.68, and 4.96 Å, respectively, representing the breakage of these Co−Sb bonds. On the atomic scale, the structural rigidity relies on the bond stiffness.[37] The breakage of Co−Sb bonds leads to the remarkably decreased structural rigidity of the $CoSb_3$/TiCoSb interface, resulting in the stress relaxation as shown in Figure 9(a). This suggests that the $CoSb_3$/TiCoSb interface can no longer resist the external deformation, representing the structural collapse and failure of the $CoSb_3$/TiCoSb interface.

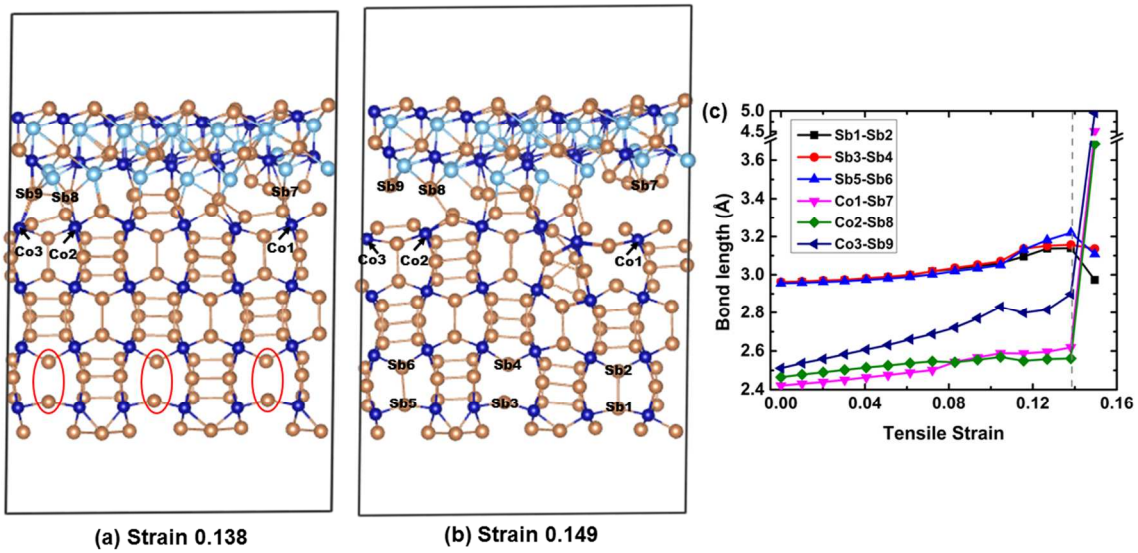

Figure 10. The atomic structures of the upper_$CoSb_3$(100)/TiCoSb(111) interface during the tensile process: (a) structure at 0.138 strain before failure strain, (b) structure at the failure strain of 0.149. The red ellipse represents the weakened or non-bonding interactions of the Sb–Sb bond. (c) The average bond lengths (Sb1–Sb2, Sb3–Sb4, Sb5–Sb6, Co1–Sb7, Co2–Sb8, and Co3–Sb9 bonds) with the increasing tensile strain during the tensile process. The gray dashed line represents the strain just before failure.

Figure 11 displays the structural deformations of the lower_$CoSb_3$(100)/TiCoSb(111) interface before and after the failure strain, respectively. Before failure, at a tensile strain of 0.094, the Sb–Sb bonds in $CoSb_3$ soften as highlighted in Figure 11(a). The structure reaches to the maximum resistance limitation because tension at this strain shows the ideal tensile strength. At the fracture strain of 0.105, the Co–Sb bonds in $CoSb_3$ such as Co1–Sb1, Co2–Sb2, and Co3–Sb3 breaks, indicating the collapse of the Co–Sb framework, resulting in the structure failure as shown in Figure 11(b). The typical bond lengths of Co1–Sb1, Co2–Sb2, Co3–Sb3, Co4–Sb4, Sb5–Sb6, and Sb7–Sb8 against tensile strains are plotted in Figure 11(c). Before the failure, the Co1–Sb1, Co2–Sb2, and Co3–Sb3 interatomic distances rapidly increase from 2.58 Å to 3.04, 3.08 and 2.97 Å, with a stretching ratio of 17.83%, 19.38%, and 15.12%, respectively, suggesting a less stable Co–Sb framework at the $CoSb_3$ boundary. The Sb5–Sb6 bond is stretched from 2.97 to 3.18 Å, representing the softening of Sb_4-rings near the interface. However, the stiffness of other Co–Sb frameworks and Sb_4-rings don't weaken too much because the Co4–Sb4 and Sb7–Sb8 bonds are only slightly stretched from 2.54 and 2.88 Å to 2.64 and 2.98 Å, respectively. At the fracture strain of 0.105, the sharply increased bond lengths of Co1–Sb1, Co2–Sb2, and

Co3–Sb3 represent structural failure, and the remarkably reduced bond lengths of Co4–Sb4, Sb5–Sb6, and Sb7–Sb8 suggest the structural recovery as well.

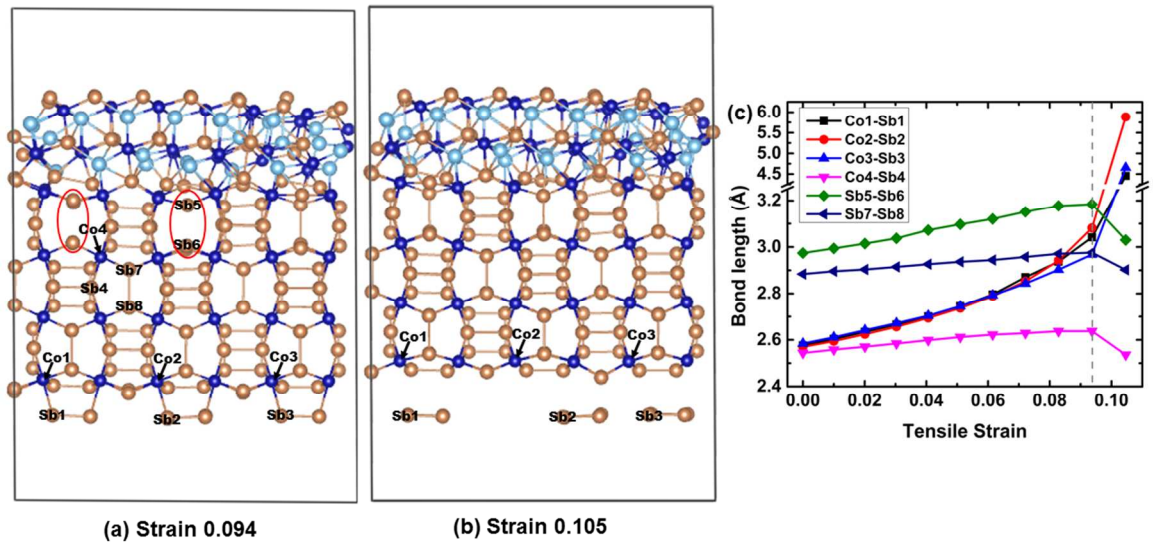

Figure 11. The atomic structures of the lower_$CoSb_3$(100)/TiCoSb(111) interface during the tensile process: (a) structure at 0.094 strain before failure strain, (b) structure at the failure strain of 0.105. The red ellipse represents the weakened or non-bonding interactions of the Sb–Sb bond. (c) The average bond lengths (Co1–Sb1, Co2–Sb2, Co3–Sb3, Co4–Sb4, Sb5–Sb6, and Sb7–Sb8 bonds) with the increasing tensile strain during the tensile process. The gray dashed line represents the strain just before failure.

Figure 12 displays the atomic structures of the upper_$CoSb_3$(100)/TiCoSb(110) interface at different applied strains. At a tensile strain of 0.072, corresponding to the ideal strength, the Co4–Sb4 bond in $CoSb_3$ breaks first, but the other Co–Sb bonds at the interfacial region such as Co1–Sb1, Co2–Sb2, and Co3–Sb3 can continue to resist the tensile deformation. With increasing tensile strain, these Co–Sb bonds soften quickly, and at a tensile strain of 0.094, the Co1–Sb1 and Co2–Sb2 bonds break. Finally, at a fracture stain of 0.105, structural failure is observed due to the breakage of the Co3–Sb3 and Sb–Sb bonds as shown in Figure 12(c). The typical lengths of these four Co–Sb bonds at various tensile strains are plotted in Figure 12(d). As the tensile strain increases to 0.041, all the Co–Sb bond lengths linearly increase, suggesting that the structure uniformly resist deformation, leading to the linearly increased tensile stress shown in Figure 9(b). At a strain of 0.051, the Co4–Sb4 bond length sharply increases from 2.83 to 3.09 Å, representing a highly softened bond and resulting in weakened structural stiffness, which explains the slightly increased tensile stress at this strain witnessed in Figure 9(b). The Co4–Sb4 bond breaks (3.44 Å)

at a strain of 0.062. At a strain of 0.083, the broken Co2–Sb2 bond (3.59 Å) and highly softened Co1–Sb1 bond (3.11 Å) lead to a decreased tensile stress at this strain, shown in Figure 9(b). Then, the tensile stress further decreases due to the breakage of Co1–Sb1 bond (3.70 Å) and softened Co3–Sb3 bond (3.12 Å) at a strain of 0.094. Finally, the breakage of Co3–Sb3 bond (4.30 Å) releases the internal stress from 3.85 to 1.20 GPa, totally collapsing the Co–Sb framework, which represents the failure of $CoSb_3$/TiCoSb interface.

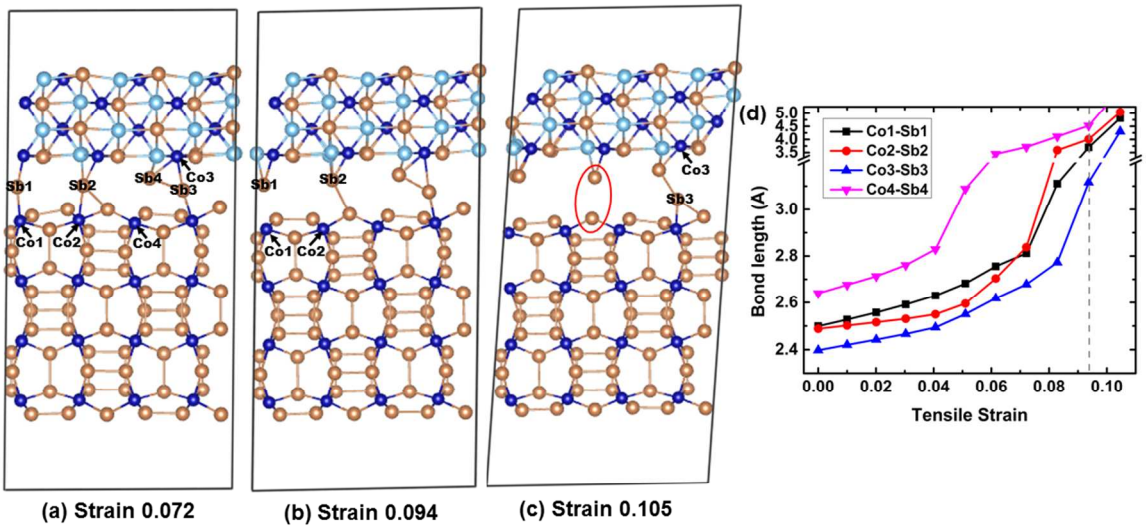

Figure 12. The atomic structures of the upper_$CoSb_3$(100)/TiCoSb(110) interface during the tensile process: (a) structure at 0.072 strain corresponding to the ideal strength, (b) structure at 0.094 strain before failure strain, (c) structure at the failure strain of 0.105. The red ellipse represents the weakened or non-bonding interactions of the Sb–Sb bond. (d) The average bond lengths (Co1–Sb1, Co2–Sb2, Co3–Sb3, and Sb2–Sb4 bonds) with the increasing tensile strain during the tensile process. The gray dashed line represents the strain just before failure.

Figure 13 displays the atomic structures of the lower_$CoSb_3$(100)/TiCoSb(110) interface and typical bond lengths at different strains. At a tensile strain of 0.061, the Co1–Sb1 and the Sb4–Sb5 interatomic distances in $CoSb_3$ sharply increase to 3.93 and 3.36 Å, suggesting the bond breaks leading to the decreased tensile stress shown in Figure 9(b). The Ti1–Sb8 bond (3.29 Å) breaks at a tensile strain of 0.083, but doesn't deconstruct the structure because the Co2–Sb2 and Co3–Sb3 bonds in the Co–Sb framework continue to resist the external deformation until a tensile strain of 0.127, shown in Figure 13(d). At a strain of 0.127 before failure, the Sb6–Sb7 bond (3.25 Å) highly softens. When the strain further increases to 0.138, the breakage of

Co2–Sb2 and Co3–Sb3 bonds collapses the Co–Sb framework, leading to the failure of the $CoSb_3$/TiCoSb interface.

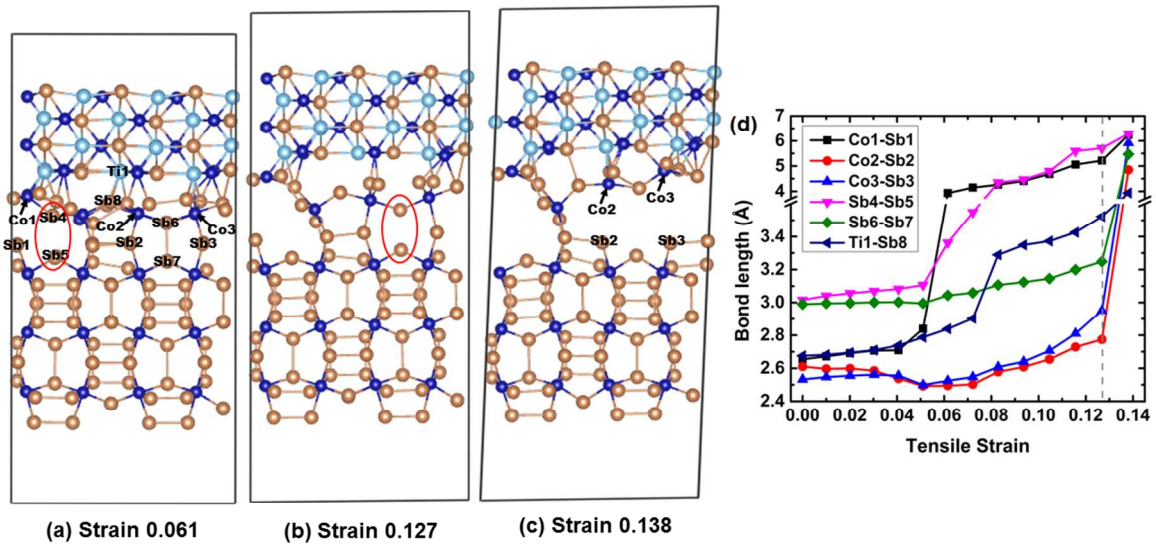

Figure 13. The atomic structures of the lower_$CoSb_3$(100)/TiCoSb(110) interface during the tensile process: (a) structure at 0.061 strain, (b) structure at 0.127 strain before failure strain, (c) structure at the failure strain of 0.138. The red ellipse represents the weakened or non-bonding interactions of the Sb–Sb bond. (d) Average bond lengths (Co1–Sb1, Co2–Sb2, Co3–Sb3, Sb4–Sb5, Sb6–Sb7, and Ti1–Sb8 bonds) with increasing tensile strain during the tensile process. The gray dashed line represents the strain just before failure.

Figures 10-13 clearly show that the collapse of the Co–Sb framework leads to the failure of the $CoSb_3$/TiCoSb interface. To enhance the ideal strength of $CoSb_3$/TiCoSb interface, we suggest improving the rigidity of the Co–Sb framework. The substitution of Sb by As could be an example of an effective way to enhance the rigidity of the Co–Sb framework because the force constant of the Co–As bond (95 N/m) is higher than that of the Co–Sb bond (85 N/m).[38] Meanwhile, the substitution of Sb by As could also decrease the CTE of $CoSb_3$,[39] reducing the CTE mismatch between $CoSb_3$ (~10.47×10^{-6} K^{-1}) and TiCoSb (8.49×10^{-6} K^{-1}) at higher temperatures,[18,39] hence decreasing the thermo-mechanical stresses in the $CoSb_3$/TiCoSb interface. Moreover, the substitution of Co by Fe could also enhance the rigidity of the Co–Sb framework because of a much higher force constant of the Fe–Sb bond (90.8 N/m) compared with that of the Co–Sb bond (85 N/m).[40]

4. CONCLUSIONS

We performed first-principles calculations based on density functional theory to illustrate the brittle mechanisms of the $CoSb_3$/TiCoSb interface. First-principles predicts that both $CoSb_3$(100)/TiCoSb(111) and $CoSb_3$(100)/TiCoSb(110) are favorable interfacial structures. The failure of the $CoSb_3$/TiCoSb interface occurs in $CoSb_3$, which agrees well with the reported experimental results. Because the rigidity of the covalent Sb−Sb bond is weaker than that of ionic Co−Sb bond, the Sb−Sb bond softens before the Co−Sb bond. The breakage of the Co−Sb bond in $CoSb_3$ leads to the failure of the $CoSb_3$/TiCoSb interface, which is similar to that of bulk $CoSb_3$. However, the ideal tensile strength of the $CoSb_3$/TiCoSb interface is much lower than that of bulk $CoSb_3$, which can be attributed to the weakened stiffness of the Co−Sb framework due to structural rearrangement near the interfacial region. To enhance the ideal strength of the $CoSb_3$/TiCoSb interface, we suggest improving the rigidity of the Co−Sb framework by use of proper substituting elements *i.e.* the substitution of Sb by As or the substitution of Co by Fe.

ACKNOWLEDGEMENTS

This work is partially supported by National Basic Research Program of China (973-program) under Project no. 2013CB632505, the 111 Project of China under Project no. B07040, Materials Project by Department of Energy Basic Energy Sciences Program under Grant No. EDCBEE, DOE Contract DE-AC02-05CH11231, National Natural Science Foundation of China (No. 11302156), and China Postdoctoral Science Foundation (408-32200031). U.A. acknowledges the financial assistance of The Scientific and Technological Research Council of Turkey. W.A.G. acknowledges the financial assistance form NSF (DMR-1436985).

Supporting information. Explanation of four named interfacial structures, and how to model possible coherent structures for the $CoSb_3$/TiCoSb interface.

REFERENCES

(1) Snyder, G. J.; Toberer, E. S. Complex Thermoelectric Materials. *Nat. Mater.* **2008**, 7, 105-114.

(2) Nolas, G. S.; Morelli, D. T.; Tritt, T. M. Skutterudites: A Phonon-Glass-Electron Crystal Approach to Advanced Thermoelectric Energy Conversion Applications. *Annu. Rev. Mater. Sci.* **1999**, 29, 89-116.

(3) Zhou, X. Y.; Wang, G. W.; Guo, L. J.; Chi, H.; Wang, G. Y.; Zhang, Q. F.; Chen, C. Q.; Thompson, T.; Sakamoto, J.; Dravid, V. P.; Cao, G. Z.; Uher, C. Hierarchically Structured TiO2 for Ba-Filled Skutterudite with Enhanced Thermoelectric Performance. *J. Mater. Chem. A.* **2014**, 2, 20629-20635.

(4) Ballikaya, S.; Uher, C. Enhanced Thermoelectric Performance of Optimized Ba, Yb Filled and Fe Substituted Skutterudite Compounds. *J. Alloys Compd*. **2014**, 585, 168-172.

(5) Rull-Bravo, M.; Moure, A.; Fernandez, J. F.; Martin-Gonzalez, M. Skutterudites as Thermoelectric Materials: Revisited. *RSC. Adv.* **2015**, 5, 41653-41667.

(6) Tang, Y. L.; Qiu, Y. T.; Xi, L. L.; Shi, X.; Zhang, W. Q.; Chen, L. D.; Tseng, S. M.; Chen, S. W.; Snyder, G. J. Phase Diagram of In–Co–Sb System and Thermoelectric Properties of In-Containing Skutterudites. *Energy Environ. Sci.* **2014**, 7, 812-819.

(7) Shi, X.; Yang, J.; Salvador, J. R.; Chi, M. F.; Cho, J. Y.; Wang, H.; Bai, S. Q.; Yang, J. H.; Zhang, W. Q.; Chen, L. D. Multiple-Filled Skutterudites: High Thermoelectric Figure of Merit through Separately Optimizing Electrical and Thermal Transports. *J. Am. Chem. Soc.* **2011**, 133, 7837-7846.

(8) Zeier, W. G.; Schmitt, J.; Hautier, G.; Aydemir, U.; Gibbs, Z. M.; Felser, C.; Snyder, G. J., Engineering Half-Heusler Thermoelectric Materials Using Zintl Chemistry. *Nat. Rev. Mater.* **2016**, 16032, 1-10.

(9) Qiu, P.; Huang, X.; Chen, X.; Chen, L., Enhanced Thermoelectric Performance by the Combination of Alloying and Doping in TiCoSb-based Half-Heusler Compounds. *J. Appl. Phys.* **2009**, 106, 103703-1 –103703-5.

(10) Li, G. D.; An, Q.; Aydemir, U.; Goddard, W. A.; Wood, M.; Zhai, P. C.; Zhang, Q. J.; Snyder, G. J., Enhanced Ideal Strength in the Thermoelectric Half-Heusler TiNiSn by Sub-Structure Engineering. *J. Mater. Chem. A.* submitted.

(11) Snyder, G. J.; Ursell, T. S., Thermoelectric Efficiency and Compatibility. *Phys. Rev. Lett.* **2003**, 91, 148301-1 – 148301-4.

(12) Bae, K. H.; Choi, S. M.; Kim, K. H.; Choi, H. S.; Seo, W. S.; Kim, I. H.; Lee, S.; Hwang, H. J. Power-Generation Characteristics After Vibration and Thermal Stresses of Thermoelectric Unicouples with $CoSb_3$ /Ti/Mo(Cu) Interfaces. *J. Electron. Mater.* **2015**, 44, 2124-2131.

(13) Zhao, D. G.; Geng, H. R.; Chen, L. D. Microstructure Contact Studies for $CoSb_3$ Thermoelectric Devices. *Int. J. Appl. Ceram. Technol.* **2012**, 9, 733-741.

(14) Zhao, D.; Li, X.; He, L.; Jiang, W.; Chen, L., High Temperature Reliability Evaluation of $CoSb_3$/electrode Thermoelectric Joints. *Intermetallics*. **2009**, 17, 136-141.

(15) Zhao, D.; Li, X.; He, L.; Jiang, W.; Chen, L., Interfacial Evolution Behavior and Reliability Evaluation of $CoSb_3$/Ti/Mo–Cu Thermoelectric Joints during Accelerated Thermal Aging. *J. Alloys Compd.* **2009**, 477, 425-431.

(16) Zhao, D.; Geng, H.; Teng, X., Fabrication and Reliability Evaluation of $CoSb_3$/W–Cu Thermoelectric Element. *J. Alloys Compd.* **2012**, 517, 198-203.

(17) El-Genk, M. S.; Saber, H. H.; Caillat, T.; Sakamoto, J. Tests Results and Performance Comparisons of Coated and Un-Coated Skutterudite Based Segmented Unicouples. *Energy Convers. Manage.* **2006**, 47, 174-200.

(18) Skovsen, I.; Bjerg, L.; Christensen, M.; Nishibori, E.; Balke, B.; Felser, C.; Iversen, B. B., Multi-Temperature Synchrotron PXRD and Physical Properties Study of Half-Heusler TiCoSb. *Dalton Trans.* **2010**, 39, 10154-10159.

(19) Li, G. D.; An, Q.; Li, W. J.; Goddard, W. A.; Zhai, P. C.; Zhang, Q. J.; Snyder, G. J., Brittle Failure Mechanism in Thermoelectric Skutterudite $CoSb_3$. *Chem. Mater.* **2015**, 27, 6329-6336.

(20) Kresse, G.; Furthmuller, J. Efficiency of ab-initio Total Energy Calculations for Metals and Semiconductors Using a Plane-Wave Basis Set. *Comput. Mater. Sci.* **1996**, 6, 15-50.

(21) Kresse, G.; Furthmuller, J. Efficient Iterative Schemes for ab initio Total-Energy Calculations Using a Plane-Wave Basis Set. *Phys. Rev. B.* **1996**, 54, 11169-11186.

(22) Kresse, G.; Joubert, D. From Ultrasoft Pseudopotentials to the Projector Augmented-Wave Method. *Phys. Rev. B.* **1999**, 59, 1758-1775.

(23) Schmidt, T.; Kliche, G.; Lutz, H. D. Structure Refinement of Skutterudite-Type Cobalt Triantimonide, $CoSb_3$. *Acta Crystallogr. C.* **1987**, 43, 1678-1679.

(24) Birkel, C. S.; Zeier, W. G.; Douglas, J. E.; Lettiere, B. R.; Mills, C. E.; Seward, G.; Birkel, A.; Snedaker, M. L.; Zhang, Y. C.; Snyder, G. J.; Pollock, T. M.; Seshadri, R.; Stucky, G. D., Rapid Microwave Preparation of Thermoelectric TiNiSn and TiCoSb Half-Heusler Compounds. *Chem Mater*. **2012**, 24, 2558-2565.

(25) Kim, H.; Kaviany, M.; Thomas, J. C.; Van der Ven, A.; Uher, C.; Huang, B. L. Structural Order-Disorder Transitions and Phonon Conductivity of Partially Filled Skutterudites. *Phys. Rev. Lett.* **2010**, 105, 265901-265901-4.

(26) Guo, R. Q.; Wang, X. J.; Huang, B. L. Thermal Conductivity of Skutterudite $CoSb_3$ from First Principles: Substitution and Nanoengineering Effects. *Sci Rep-Uk.* **2015,** *5*, 7806-7806-9.

(27) Sun, G.; Li, Y.; Zhao, X.; Mi, Y.; Wang, L., First-Principles Investigation of the Effect of M-Doped (M = Zr, Hf) TiCoSb Half-Heusler Thermoelectric Material. *J. Mater. Sci. Chem. Eng.* **2015**, 03, 78-86.

(28) Hao, S.; Delley, B.; Stampfl, C., Structure and Properties of TiN(111)/Si_xN_y/TiN(111) Interfaces in Superhard Nanocomposites: First-Principles Investigations. *Phys. Rev. B.* **2006**, 74, 035402-1-035402-12.

(29) Hao, S.; Delley, B.; Veprek, S.; Stampfl, C., Superhard Nitride-based Nanocomposites: Role of Interfaces and Effect of Impurities. *Phys. Rev. Lett.* **2006**, 97, 086102-1-086102-4.

(30) An, Q.; Goddard, W. A.; Cheng, T. Atomistic Explanation of Shear-Induced Amorphous Band Formation in Boron Carbide. *Phys. Rev. Lett.* **2014**, 113, 095501-095501-5.

(31) Ogata, S.; Li, J.; Yip, S. Ideal Pure Shear Strength of Aluminum and Copper. *Science.* **2002**, 298, 807-811.

(32) Roundy, D.; Krenn, C. R.; Cohen, M. L.; Morris, J. W. Ideal Shear Strengths of fcc Aluminum and Copper. *Phys. Rev. Lett.* **1999**, 82, 2713-2716.

(33) Hao, S.; Delley, B.; Stampfl, C., Role of Oxygen inTiN(111)/Si_xN_y/TiN(111) Interfaces: Implications for Superhard Nanocrystalline *nc*−TiN/*a*−Si_3N_4 Nanocomposites. *Phys. Rev. B.* **2006**, 74, 035424-1-035424-10.

(34) Ouardi, S.; Fecher, G. H.; Balke, B.; Kozina, X.; Stryganyuk, G.; Felser, C.; Lowitzer, S.; Kodderitzsch, D.; Ebert, H.; Ikenaga, E., Electronic Transport Properties of Electron- and Hole-Doped Semiconducting $C1_b$ Heusler Compounds: $NiTi_{1-x}M_xSn$ (*M*=Sc, V). *Phys. Rev. B.* **2010**, 82, 085108-1-085108-9.

(35) Ooi, N.; Rairkar, A.; Adams, J. B., Density Functional Study of Graphite Bulk and Surface Properties. *Carbon.* **2006**, 44, 231-242.

(36) Li, G. D.; Bajaj, S.; Aydemir, U.; Hao, S,; Xiao, H.; Goddard, W. A.; Zhai, P. C.; Zhang, Q. J.; Snyder, G. J., p-Type Co Interstitial Defects in Thermoelectric Skutterudite $CoSb_3$ Due to the Breakage of Sb_4-Rings. *Chem. Mater.* **2016**, 28, 2172-2179.

(37) Li, G. D.; An, Q.; Aydemir, U.; Goddard, W. A.; Wood, M.; Zhai, P. C.; Zhang, Q. J.; Snyder, G. J., Enhanced Ideal Strength in the Thermoelectric Half-Heusler TiNiSn by Sub-Structure Engineering. *J. Mater. Chem. A.* **2016**, 4, 14625-14636.

(38) Lutz, H. D.; Kliche, G., Far-Infrared Reflection Spectra of CoP_3, $CoAs_3$, $CoSb_3$. *Phys. Status Solidi B.* **1982**, 112, 549-557.

(39) Rogl, G.; Rogl, P., Mechanical Properties of Skutterudites. *Sci. Adv. Mater.* **2011**, 3, 517-538.

(40) Feldman, J. L.; Singh, D. J.; Kendziora, C., Lattice Dynamics of Filled Skutterudites: $La(Fe, Co)_4Sb_{12}$. *Phys. Rev. B.* **2003**, 68, 094301-1 – 094301-11.

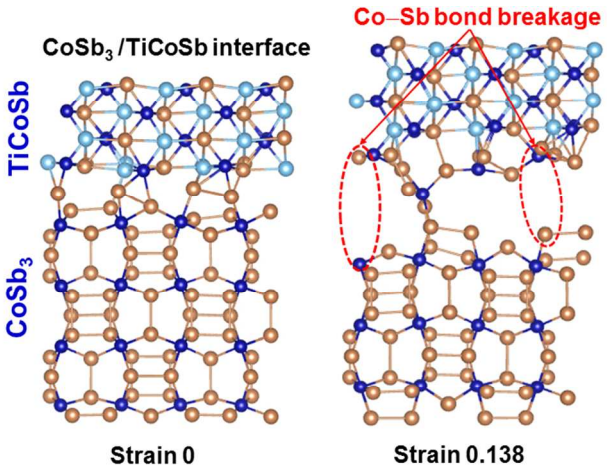

Table of Contents Graphic

304x203mm (96 x 96 DPI)